Experimental study of non-bonded packed bed active magnetic regenerators with stabilized La(Fe,Mn,Si)$_{13}$H$_y$ particles

Jierong Liang [a,*], Marvin Masche [a], Kurt Engelbrecht [a], Kaspar K. Nielsen [a,1], Hugo A. Vieyra [b], Alexander Barcza [b], Christian R.H. Bahl [a]

[a] Department of Energy Conversion and Storage, Technical University of Denmark, Anker Engelunds Vej, 2800 Kgs. Lyngby, Denmark
[b] Vacuumschmelze GmbH & Co. KG, Grüner Weg 37, 63450 Hanau, Germany

ARTICLE INFO

ABSTRACT

The aim of this study is to develop more stable magnetocaloric regenerators, made from non-epoxy-bonded La (Fe,Mn,Si)$_{13}$H$_y$ particles to address the instability issues of conventional regenerators with a first-order phase transition. The stabilized magnetocaloric materials are obtained by increasing the $\alpha - $ Fe content at the expense of a small reduction of the adiabatic temperature change. However, the experimental results show that the non-bonded structure improves the regenerator efficiency and reduces pressure drop, potentially compensating for the reduction of the material's magnetocaloric effect. Compared to epoxy-bonded regenerators, non-bonded regenerators exhibit a larger temperature span (10.2 K at no load) and specific cooling power (27% improvement at a span of 4 K). Due to the elimination of the epoxy, a lower friction factor and higher packing density are obtained. The long-term mechanical and chemical stabilities are verified by comparing specific heat, effectiveness, and pressure drop before and after a test period of more than one year.

1. Introduction

Caloric technologies, being alternatives to vapor compression refrigeration at room temperature, have been widely studied in recent decades [1–5]. To realize the potential benefits of caloric cooling and heating, which includes the use of environmentally friendly refrigerants, high efficiency, and lower noise, the interdisciplinary knowledge related to material science [6–9], magnetic system design [10–12], and thermodynamics [13–15] is highly desired to develop high-performance prototypes [16–20]. As a pioneer caloric application, magnetocaloric refrigeration has been developed mostly based on the active magnetic regenerator (AMR, [21]). AMRs exhibit the magnetocaloric effect (MCE) by magnetocaloric materials (MCMs) and simultaneously enable heat regeneration along the length of the solid refrigerant [22]. The heat regeneration substantially increases the temperature span otherwise limited by the adiabatic temperature change of the MCM. In addition to the thermal–hydraulic investigations [23–26], it is also central for researchers to focus on the stability and efficiency of MCMs that are used in AMRs [27–29].

MCMs can either undergo a first-order phase transition (FOPT) with

a discontinuity in the first derivative of the Gibbs free energy, or a second-order phase transition (SOPT) with a continuous variation of the Gibbs free energy derivative [30]. Despite its outstanding MCE, the SOPT benchmark material gadolinium (Gd) is not a highly attractive option for widespread application due to its scarcity and cost. FOPT materials exhibit comparatively larger isothermal entropy changes over narrower temperature ranges. The narrow operating range is addressed by layering several MCMs with sequential transition temperatures [31–33]. Thus, FOPT materials can be considered as the better-performing and lower-cost alternatives to Gd.

La(Fe,Mn,Si)$_{13}$H$_y$ alloys with tunable transition temperatures and high MCE are among the most promising materials that go through FOPT with low hysteresis and are commercially available [34]. Aprea et al. [35] numerically showed that using La(Fe,Mn,Si)$_{13}$H$_y$ in an AMR cycle results in a better total equivalent warming impact than when using a SOPT material. However, FOPT materials are less widely available in AMR-scale testing compared to common SOPT materials [31]. The characterization of AMRs with La(Fe,Mn,Si)$_{13}$H$_y$ is one of the most active research areas within AMR technology. Bez et al. [36] comparatively studied packed irregular La(Fe,Mn,Si)$_{13}$H$_y$ regenerators with and without epoxy bonding. The regenerators without epoxy exhibit better

Nomenclature

Abbreviations

AMR	Active magnetic regenerator
DSC	Differential scanning calorimetry
EDS	Energy dispersive spectroscopy
FOPT	First-order phase transition
Gd	Gadolinium
MCE	Magnetocaloric effect
MCM	Magnetocaloric material
SEM	Scanning electron microscope
SOPT	Second-order phase transition

Variables

c	Specific heat capacity, [J kg^{-1} K^{-1}]
D_h	Hydraulic diameter, [m]
D_{sp}	Average particle diameter, [m]
f	Frequency, [Hz]
f_F	Fanning friction factor, [-]
m	Mass, [kg]
L	Length, [m]
p	Pressure, [Pa]
Re_h	Reynolds number based on hydraulic diameter, [-]
T	Temperature, [K]

t	Time, [s]
U	Utilization, [-]
v_f	Fluid superficial flow velocity, [m/s]

Greek symbols

a	Specific surface area, [m^{-2}]
Δ	Difference
ΔT_0	No-load temperature span, [K]
ϵ	Porosity, [-]
η	Effectiveness, [-]
μ	Dynamic viscosity, [Pa·s]
ρ	Density, [kg m^{-3}]
τ	Period time, [s]

Subscripts

ad	Adiabatic
c	Cold end or cold-to-hot blow
C	Curie point
f	Fluid
h	Hot end or hot-to-cold blow
max	Maximum or amplitude
r	Regenerator
s	Solid

performance than epoxy-bonded ones, and almost no difference in no-load temperature span is observed between regenerators with and without epoxy. However, the regenerators without epoxy broke apart after a three-week test, probably due to the magnetovolume effect and fluid oscillation. Navickaité et al. [37] tested an epoxy addition of 2 wt% to balance the mechanical integrity and MCM/heat transfer performance and obtained temperature spans of above 20 K for five- and nine-layer La(Fe,Mn,Si)$_{13}$H$_y$ regenerators. Lei et al. [26] obtained a no-load temperature span of 16.8 K for five-layer epoxy-bonded regenerators with spherical La(Fe,Mn,Si)$_{13}$H$_y$ particles. They validated the stability of regenerators by a four-month static corrosion test and a two-month period where the regenerator was tested through multiple experiments. Recently, Vieira et al. [38] investigated epoxy-bonded La(Fe,Mn,Si)$_{13}$H$_y$ AMRs with larger α − Fe content to ensure mechanical integrity. They obtained a no-load temperature span of 12 K for a three-layer AMR.

Thus, La(Fe,Mn,Si)$_{13}$H$_y$ AMRs can provide considerable performance, but they are accompanied by practical challenges concerning mechanical stability.

One solution to the brittleness of La(Fe,Mn,Si)$_{13}$H$_y$ is the aforementioned polymer bonding [39]. As pointed out in Ref. [38], epoxy-bonding resulted in both lower thermal conductivity and reduced effective specific heat transfer area. Due to the magnetovolume effect near the transition temperature, alternating thermal and mechanical stresses result in aging and fatigue of the epoxy adhesive [40,41]. Radulov et al. [42,43] presented a metal-bonding technique for La(Fe, Mn,Si)$_{13}$H$_y$. Both a stable MCE and excellent corrosion resistance were obtained at the expense of a relatively high time constant for heat transfer, which limits the operating frequencies. There is a need to minimize the side effect of the attempts to address the mechanical stability of La(Fe,Mn,Si)$_{13}$H$_y$ AMRs. An important drawback for FOPT

Table 1
Regenerator configuration parameters and test scheme.

Parameters	Epo-HS	Sph1-HS	Irr1-H	Irr2-H
Shape (ØD × L, mm × mm)	Ø22.6 × 40	Ø22.6 × 40	Ø30 × 40	Ø22.6 × 40
Particle shape	Spheres	Spheres	Irregular particles	Irregular particles
Particle size (μm) †	400–640 (505)	400–640 (505)	250–450 (350)	100–250 (200)
Total porosity	~0.465	0.491	0.505	0.545
Hydraulic diameter (μm)	293	325	238	160
Specific surface area (m^{-1})	6356	6048	8486	1.365×10^4
Material	CALORIVAC-HS	CALORIVAC-HS	CALORIVAC-H	CALORIVAC-H
Mass (g)	59.2	56.3	82.1	50.4
Epoxy-bonded	√	×	×	×
Passive test	√	√	√	√
Active test	√	√	×	×
Photos‡				

† The size ranges come from the manufacturer that were analyzed using the sieve analysis. The average values in parentheses are determined from measuring average mass per particle, which are used as D_{sp} in Eq. (1).

‡ The picture of Sph1-HS was taken from a smaller housing for demonstration purposes and therefore was framed differently than the others.
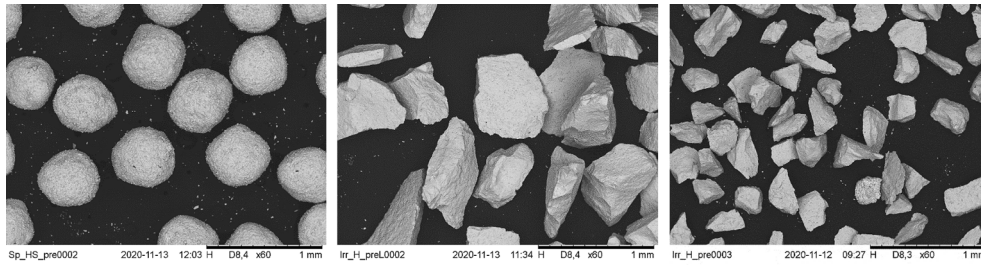
Fig. 1. SEM micrographs of the microstructures of Sph1-HS particles (left), the Irr1-H irregular particles of 250–450 μm (middle), and the Irr2-H irregular particles of 100–250 μm (right).

materials is the possibly significant change in the magnetocaloric response under cyclic measurements [44,45]. Thus, studying the reversibility of MCM candidates in periodic magnetocaloric systems is valuable.

In this study, we investigate the potential of non-bonded AMRs with La(Fe,Mn,Si)$_{13}$H$_y$ stabilized by increasing the $\alpha - $Fe content. The MCE parameters between original and stabilized La(Fe,Mn,Si)$_{13}$H$_y$ are compared. Performance experiments are carried out for epoxy-bonded and non-bonded AMRs made from the original and stabilized La(Fe, Mn,Si)$_{13}$H$_y$. As will be shown below, the non-bonded La(Fe,Mn,Si)$_{13}$H$_y$ AMRs can outperform the epoxy-bonded one and only minor degradation of performance is observed from the stabilizing of the La(Fe,Mn, Si)$_{13}$H$_y$. Mechanical stability and magnetocaloric reversibility of the non-bonded AMRs are evaluated by the comparison of scanning electron microscope (SEM) images, specific heat curves, as well as comparing pressure drop and heat transfer effectiveness after prolonged testing.

2. Regenerator preparation and experiment description

Two classes of La(Fe, Mn, Si)$_{13}$H$_z$ alloys, namely CALORIVAC-H with original stoichiometry and CALORIVAC-HS with larger $\alpha - $Fe content, were produced by Vacuumschmelze GmbH & Co. using powder metallurgy and hydrogenation, which are described in Refs. [34,46,47]. Particles of the materials were packed into four regenerators as shown in Table 1. All the regenerators in this study are designed as a single layer of MCMs to focus on the effect of epoxy and $\alpha - $Fe addition. The particle size ranges stated in Table 1 were obtained by sieve analysis, and the data were provided by the manufacturer. It is important to note that all regenerators had the same diameters, except for Irr1-H, which was only used for thermal–hydraulic characterization. Varying porosities were obtained due to the limitations of manual packing. The relatively high porosities of Irr1-H and Irr2-H are attributed to the relatively high irregularity of the particle shapes [36], which can also be observed in the SEM images in Section 3. The geometrical parameters in Table 1 are derived from the average particle diameter and the porosity,

$$D_h = \frac{2\epsilon}{3(1-\epsilon)}D_{sp} \tag{1}$$

$$\alpha = \frac{4\epsilon}{D_h} \tag{2}$$

where ϵ, D_{sp}, D_h and α denote porosity, average particle diameter, hydraulic diameter and specific surface area, respectively.

The MCMs for Epo-HS and Sph1-HS are spherical particles with and without epoxy, respectively. They are from the same batch, which can be assumed to have the same MCE, while the irregular CALORIVAC-H particles (Irr1-H and Irr2-H) are from different batches. For further investigation shown in Section 4, Sph1-HS will be repacked to Sph2- and Sph3-HS with different porosities and dimensions, and Irr1-H will be repacked to Irr3-H due to the failures.

The passive characterization is carried out in a specially built regenerator tester [26], including regenerator assembly, heater and heat

exchanger, piston and motor assembly, check valves, and tubing. Characteristics of heat transfer and flow resistance are evaluated by subjecting the regenerators to an oscillating flow with constant reservoir temperatures (T_h and T_c) and without a magnetic field. The operating parameters consist of motor frequency, piston stroke and piston diameter, which determine the fluid flow waveforms. The main measurements are pressure drop (Δp) and end temperatures ($T_{f,h}$ and $T_{f,c}$). Heat transfer effectiveness associated with the hot-to-cold blow (η_h), thermal utilization (U), Reynolds number (Re$_h$), and Fanning friction factor (f_F) are adopted as dimensionless metrics [48],

$$\eta_h = \frac{T_h - 2/\tau \int_{\tau/2}^{\tau} T_{f,c} dt}{T_h - T_c} \tag{3}$$

$$U = \frac{\int_0^{\tau/2} \dot{m}_f c_f dt}{m_s c_s} \tag{4}$$

$$\mathrm{Re}_h = \frac{\rho_f \left(v_{f,max}/\epsilon\right)D_h}{\mu_f} \tag{5}$$

$$f_F = \frac{\Delta p_{max}}{L_r}\frac{D_h}{2\rho_f \left(v_{f,max}\right)^2} \tag{6}$$

Note that the Reynolds number is based on the interstitial velocity ($v_{f,max}/\epsilon$). The value of c_s used for the utilization definition is 500 J•kg^{-1}•K^{-1} based on the background value. For the passive regenerator tester, the uncertainties for temperature and pressure measurements are less than 3 %, as reported in [49].

The active characterization is performed in a small-scale AMR test machine with a frequency of $\sim$ 0.12 Hz, as described in Ref. [50]. The test machine consists of a fixed Halbach cylindrical permanent magnet with a maximum field of 1.1 T, a reciprocating movable regenerator, and an oscillatory flow subsystem. The temperature span is obtained from the hot and cold reservoir temperatures and the cooling capacity is simulated from the power of an electric heater. The reservoir temperatures are measured with calibrated E-type thermocouples and with a measurement error of $\pm$ 0.5 K. As the maximum performance is generally found when the midpoint of the end temperatures approaches the material transition temperature [51], the working temperature is defined as the average of the hot and cold reservoir temperatures in this study.

For both passive and active characterizations, the heat transfer fluid is a water solution with a $\sim$ 2% volumetric fraction of the corrosion inhibitor ENTEK. The passive and active testing of the regenerators is summarized in Table 1.

3. Magnetocaloric material

To investigate the feasibilities of modifying the original La(Fe,Mn, Si)$_{13}$H$_y$ with a higher $\alpha - $Fe content, MCMs in Table 1 were characterized by scanning electron microscope (SEM) with Energy dispersive spectroscopy (EDS), in-field specific heat (c_s) and adiabatic temperature change (ΔT_{ad}). Fig. 1 shows the SEM micrographs of samples from Sph1-
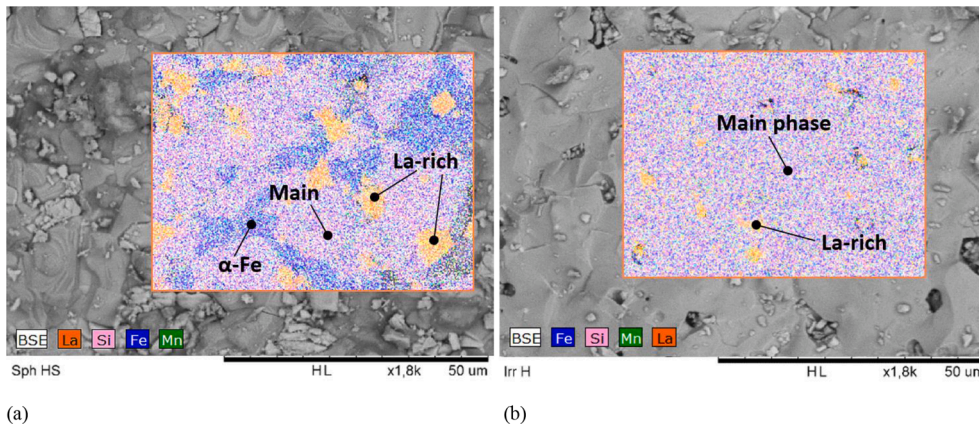
Fig. 2. SEM with EDS analysis for (a) a Sph1-HS particle and (b) an Irr-H particle.

Table 2
Quantitative elemental compositions estimated from EDS mapping of the MCM samples. The values represent weight (wt.) percentages that have been normalized to 100%, and with one standard deviation (above and below).

	Sph1-HS				Irr1-H		
	Average	Main phase	La-rich phase	α-Fe phase	Average	Main phase	La-rich phase
Fe	75.0 ± 2.3	76.7 ± 2.3	27.5 ± 0.8	89.1 ± 2.6	76.4 ± 2.2	77.7 ± 2.2	43.6 ± 1.2
La	20.30 ± 0.6	17.83 ± 0.5	70.7 ± 2.0	7.22 ± 0.2	17.41 ± 0.5	16.37 ± 0.5	52.8 ± 1.4
Si	3.06 ± 0.2	3.84 ± 0.2	1.19 ± 0.1	1.60 ± 0.1	4.53 ± 0.2	4.28 ± 0.2	2.59 ± 0.1
Mn	1.63 ± 0.1	1.68 ± 0.1	0.66 ± 0.0	2.12 ± 0.1	1.67 ± 0.1	1.66 ± 0.1	0.98 ± 0.1

HS, Irr1-H, and Irr2-H. The images clearly illustrate the different morphologies of the MCM samples. Sph1-HS particles are mostly spherical and have a uniform size with a diameter of about 0.5 mm, while the different size ranges of Irr1-H and Irr2-H particles have a very irregular morphology.

In Fig. 2, the SEM with EDS analysis suggests that the Sph-HS particles contain three phases: the main La(Fe,Mn,Si)$_{13}$H$_z$ phase (light gray), the α-Fe phase (dark gray), and a La-rich phase (white). It also confirms the presence of the ductile $\alpha - Fe$ in Sph-HS particles, which has previously been shown to act as a toughening phase in the Fe-rich alloy and improve its mechanical stability, thus enhancing the

material lifetime [52]. This $\alpha - Fe$ phase is not observed in the Irr-H particles, where only two phases, i.e., the La-rich phase and the main magnetocaloric phase are identified. The relative chemical compositions of the different sample phases measured by EDS are presented in Table 2. According to the material producer, the amount of the $\alpha - Fe$ phase was determined by magnetic measurements to be ∼ 17 vol% in the Sph-HS and ∼ 4 vol% in the Irr-H particles. Using a vibrating sample magnetometer (LakeShore 7407), samples of both materials were measured at 350 K. Assuming a saturation magnetization of the α-Fe of 2.2 T and subtracting the paramagnetic contribution we find values of 15 vol% in the Sph-HS and 2 vol% in the Irr-H particles. In the EDS analysis, the lack of identified $\alpha - Fe$ phase in the Irr-H sample may be due to smaller areas, and the very low fraction.

Fig. 3 shows the specific heat of particles taken from Sph1-HS and Irr1-H each with a sample mass of ∼ 3 mg (equivalent to about 10 particles). In Fig. 3 (a), the specific heat curves of CALORIVAC-HS spheres exhibit shallow lambda-like cusps over the transition temperature, characteristic of a so-called weak FOPT between paramagnetic and ferromagnetic states. In Fig. 3 (b), the specific heat curves of CALORIVAC-H irregular particles show sharp peaks and therefore relatively strong FOPT characteristics. The observed multiple peaks in the specific heat curve at zero field in Fig. 3 (b) are probably due to variations in the local chemical composition from particle to particle [53]. The shift of the transition temperature with the field $\Delta T_c / \Delta H$ for samples from Sph1-HS and Irr1-H is found to be ∼ 6.0 and ∼ 5.1 K/T, respectively. These values are consistent with Ref. [53].

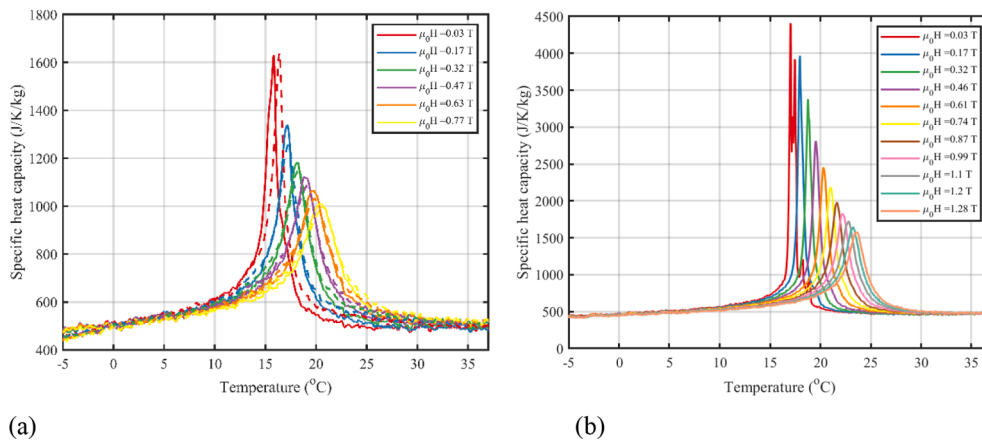After periodic hydraulic and magnetocaloric operation for about

Fig. 3. Specific heat curves for (a) CALORIVAC-HS spheres from Sph1/Sph2/Sph3-HS and (b) CALORIVAC-H irregular particles from Irr1/Irr3-H. The specific heat of CALORIVAC-HS spheres was remeasured after testing (dashed lines) and compared to the initial values in subfigure (a). The data were obtained from an in-field differential scanning calorimetry (DSC) with a measurement error of up to 7.5 % [54,55].
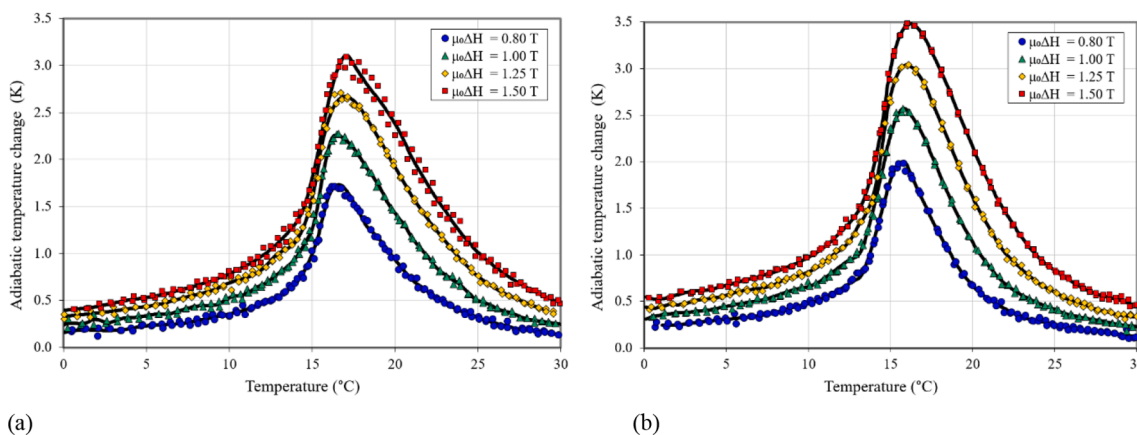
Fig. 4. The data of adiabatic temperature change under various magnetic fields for (a) CALORIVAC-HS spheres from Sph1-HS and (b) CALORIVAC-H irregular particles from Irr1-H. The data were provided by the manufacturer and were measured using an in-house device designed and constructed at Vacuumschmelze, which recorded the temperature change of a sample between the field and no field positions of a rotating magnetic system.
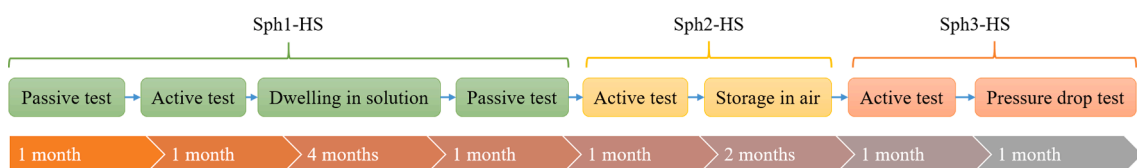

Fig. 5. The schematic diagram for testing the packed sphere regenerator from Sph1-HS to Sph3-HS.

eight months, as well as long term storage for about four months (illustrated in Fig. 5), the repeated specific curves for some magnetic fields are shown as dashed lines in Fig. 3 (a). A slight shift of the curve is observed probably due to the variations in the local chemical composition across the samples taken from different particles in Sph1-HS. No significant change in the specific heat peaks is captured. Thus, the chemical stability of CALORIVAC-HS is confirmed.

The MCE comparison between the CALORIVAC-HS spheres and CALORIVAC-H irregular particles is evaluated via ΔT_{ad} shown in Fig. 4. Under the magnetic field change from 0 T to 1 T, the ΔT_{ad} amplitude of CALORIVAC-HS spheres is 2.25 K compared to 2.5 K in CALORIVAC-H irregular particles.

4. Results and discussion

The regenerators listed in Table 1 were evaluated in terms of heat transfer effectiveness, friction factor, cooling capacity and stability by repeating passive and active tests after prolonged periods. Irr1-H and Irr2-H failed to survive the passive test after a few days of running due to a failure of the screen mesh holding the particles in the regenerator. Thus, the material of Irr1-H was reused to produce another AMR Irr3-H for active testing. As will be seen in Section 4.3, the cooling performance of Sph1-HS is not promising due to a low packing quality. We reproduced AMRs Sph2-HS and Sph3-HS using the MCMs from Sph1-HS to investigate the effect of enhancing the packing quality. The packing quality was enhanced by compressing the MCMs and improving the waterproofing with new glue. Each reproduction involves the steps of (i) disassembling the regenerator, (ii) drying the particles in air for about three days, and (iii) refilling. The schematic diagram for the test history from Sph1-HS to Sph3-HS is shown in Fig. 5. For brevity, Sph2-HS and Sph3-HS skipped the full passive test and focused on the cooling performance sensitivity and stability as shown in Section 4.3. However, the pressure drop was still tested for Sph3-HS in Section 4.2 to investigate the potential of non-bonded regenerators with a higher packing density. The parameters for all reproduced AMRs are summarized in Table 3.

Table 3
Reproduced regenerator configuration parameters.

Parameters	Sph2-HS	Sph3-HS	Irr3-H
Shape (ØD × L, mm × mm)	Ø22.6 × 34	Ø22.6 × 40	Ø22.6 × 40
Particle shape	Spheres	Spheres	Irregular particles
Particle size (μm)	400–640	400–640	250–450
Total porosity	0.415	0.405	0.490
Hydraulic diameter (μm)	239	229	224
Specific surface area (m^{-1})	6950	7069	8743
Material	CALORIVAC -HS	CALORIVAC -HS	CALORIVAC -H
Mass (g)	55.0	65.8	56.4

4.1. Heat transfer effectiveness

The values of heat transfer effectiveness with respect to the utilization for the regenerators Epo-HS, Sph1-HS, Irr1-H and Irr2-H are compared in Fig. 6. Regenerator Epo-HS exhibited significantly lower effectiveness compared to the other regenerators. The reasons can be twofold: (i) reducing the specific surface area through narrowing the flow passages [38] and (ii) imposing extra thermal resistance of the solid–fluid interface [56]. For the AMRs without epoxy addition, packed irregular samples Irr1-H and Irr2-H outperformed the packed sphere Sph1-HS on effectiveness, probably due to (i) less intense tortuosity-induced fluid mixing [26,57] and (ii) larger hydraulic diameter [24] in Sph1-HS. According to the values of effectiveness in Fig. 6 and the values of hydraulic diameters in Table 1, the effects of hydraulic diameter on effectiveness become significant at higher utilization. Thus, the AMRs can be sorted for heat transfer effectiveness ranking from high to low as: Irr2-H, Irr1-H, Sph1-HS, and Epo-HS.
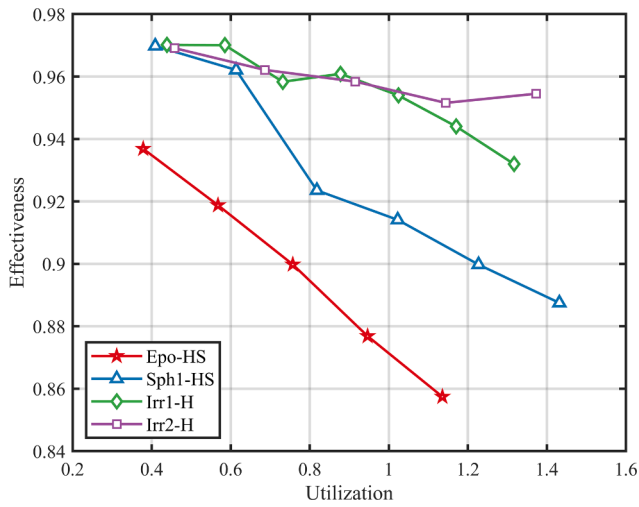
Fig. 6. Effectiveness as a function of utilization for various regenerators. The frequency and temperature span are 1 Hz and 10 K, respectively.
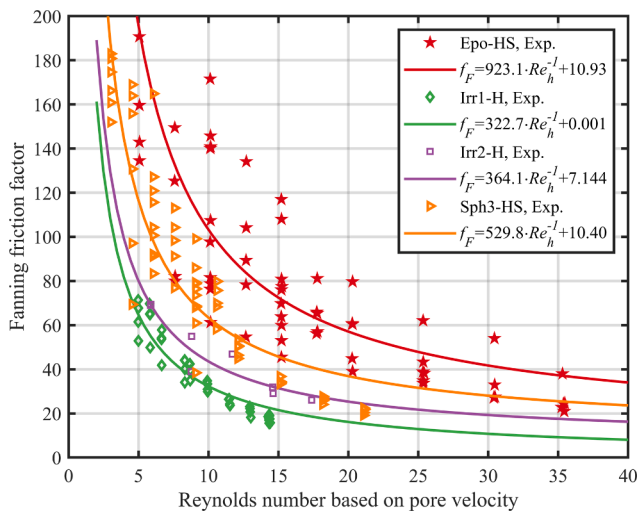

Fig. 7. Fanning friction factor as a function of Reynolds number for the regenerators Epo-HS, Irr1-H, Irr2-H and Sph3-HS.

4.2. Friction factor

The dimensionless relationship of f_F Re_h for various regenerators is shown in Fig. 7. The data spread in Epo-HS and Sph3-HS is larger than that in Irr1-H and Irr2-H, which is attributed to the temperature-dependent viscosity of the fluid. For Epo-HS and Sph3-HS, multiple working temperatures are applied in the test; while Irr1-H and Irr2-H are only tested at a single working temperature due to the aforementioned failure of the screen mesh holding the particles. The friction factor is derived from pressure drop and normalized by hydraulic diameter, regenerator length and flow velocity, which can be written in the form of $f_F = c_1 Re_h^{-1} + c_2$ as detailed in Ref. [58]. Note that the coefficients c_1 and c_2 physically indicate the viscous and inertial forces. For the cases of Re_h approaching infinity, the viscous forces are negligible, while the inertial forces govern. As the coefficients c_1 and c_2 are fitted based on the range of the experimental data, the limiting range in terms of Re_h for this f_F equation is assumed the same range as the experimental data shown in Fig. 7. The y-intercept term c_2 for all the regenerators in Fig. 7 is low, which indicates a subtle effect of inertial forces due to relatively low Re_h. The slope term c_1 indicates the permeability and dominates the value for the friction factor. From Fig. 7, Irr1-H and Irr2-H with similar c_1 values
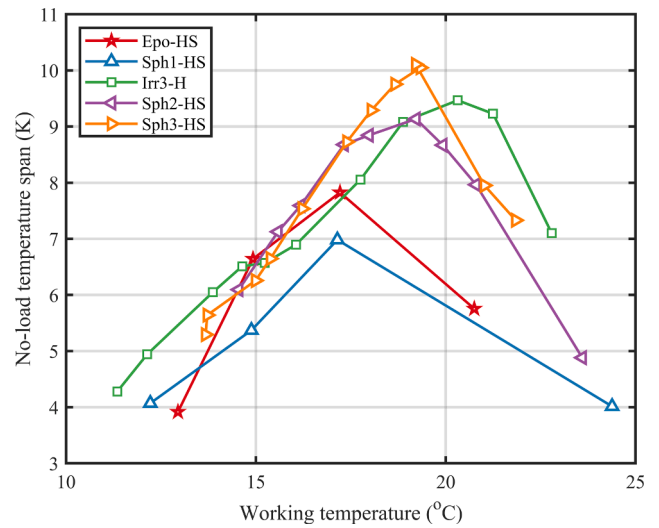

Fig. 8. No load temperature span for AMRs at a fluid displacement velocity of 3 mm/s and a displacement stroke of 7.5 mm.

have a lower friction factor than Sph3-HS and Epo-HS because of higher porosities. Comparing the friction factor between Sph3-HS and Epo-HS, it is found that Sph3-HS with more MCM still exhibits lower friction (i.e., a higher permeability) than Epo-HS. Thus, one advantage for non-bonded regenerators is the significant reduction of the flow resistance.

4.3. Cooling capacity

The influence of the working temperature on the no-load temperature span (ΔT_0) was measured by varying the hot reservoir temperatures as shown in Fig. 8. All the curves in Fig. 8 exhibit a significant sensitivity of ΔT_0 on the working temperatures due to the nature of first-order MCMs.

Comparing the ΔT_0 between Sph2-HS and Sph3-HS with the same diameter and very similar porosity, the longer regenerator is found to increase the temperature span to some extent in the vicinity of the transition temperature. However, this is a subtle effect at the working temperatures where the MCE is relatively weak. Comparing the ΔT_0 between Sph1-HS and Irr3-H with similar porosities, Sph1-HS significantly underperformed Irr3-H, which is probably attributed to both relatively lower MCE (Fig. 4) and lower heat transfer effectiveness (Fig. 6) in Sph1-HS. Note that the effectiveness of Irr3-H is expected to be similar to that of Irr1-H shown in Fig. 6, as they have the same MCMs and similar porosities. The Sph3-HS regenerator obtained the largest ΔT_0 of 10.2 K, because it is configured with less internal dead volume (low porosity) and without the heat resistant epoxy. As will be seen in Section 4.4, the non-bonded regenerator with CALORICVAC-H is not mechanically stable. As the epoxy-bonded AMRs naturally have relatively high total porosities due to the epoxy occupation, epoxy elimination in non-bonded AMRs with CALORICVAC-H can compensate for the reduction of MCE relative to epoxy-bonded AMRs with CALORICVAC-H, but the packing density of MCMs should be controlled to avoid the parasitic losses.

The sensitivity of ΔT_0 on the working conditions can be analyzed by varying the fluid displacement velocity (v_f) and the utilization (U) in Fig. 8. The blow period and v_f are in inversely related based on the constant piston diameter and displacement. Thus, varying v_f directly affects the operating frequency. As the periods of (de)magnetization are unchanged due to the reciprocating nature of the active test machine, the variation of operating frequencies by varying v_f is limited – the frequencies of 0.09 to 0.16 Hz correspond to the v_f of 3 to 10 mm/s. In Fig. 9 (a), the sensitivity of ΔT_0 on U for Epo-HS is higher than those for the other AMRs. In Fig. 9 (b), the Sph3-HS exhibited the least
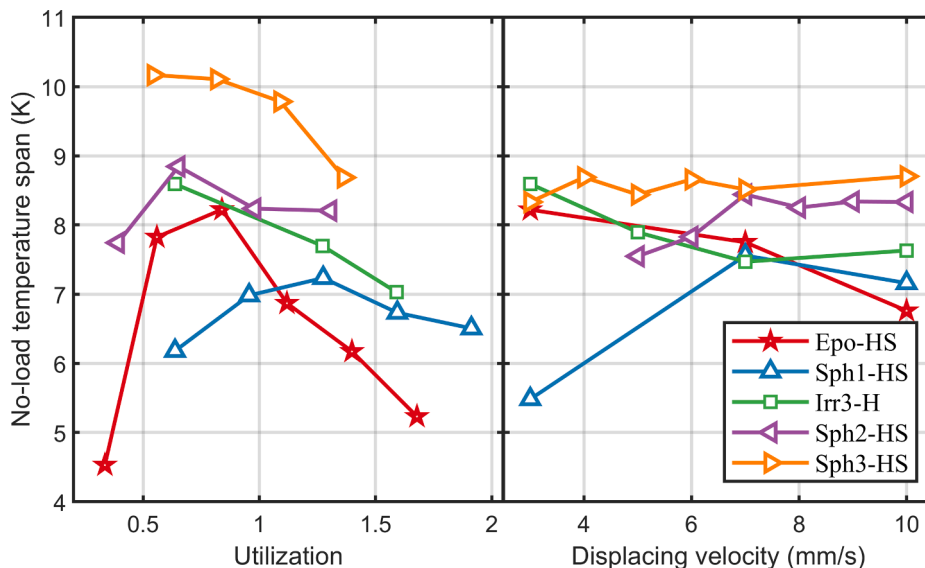
Fig. 9. The no-load temperature variation caused by varying (a) utilization and (b) displacement velocities.
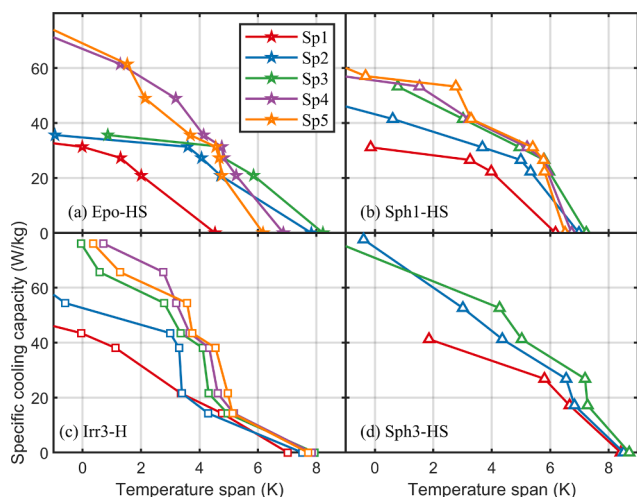

Fig. 10. Cooling curves for the regenerators of (a) Epo-HS, (a) Sph1-HS, (a) Irr3-H, and (a) Sph3-HS at different fluid strokes. Sp1, Sp2, Sp3, Sp4 and Sp5 stand for the strokes of 5 mm, 7.5 mm, 10 mm, 12.5 mm and 15 mm, respectively. Based on these fluid strokes, the utilizations of Epo-HS are 0.559, 0.839, 1.12, 1.40 and 1.68; the utilizations of Sph1-HS are 0.637, 0.956, 1.28, 1.59 and 1.91; the utilizations of Irr3-H are 0.639, 0.958, 1.28, 1.60 and 1.92; the utilizations of Sph3-HS are 0.545, 0.812 and 1.09.

dependence of ΔT_0 on v_f. The above sensitivity pattern can be attributed to the regenerator effectiveness characteristics. Based on the fixed geometrical parameters, the regeneration ratio [59,60] can be theoretically estimated to increase with the regenerator effectiveness ($\frac{\Delta T_0}{\Delta T_{ad}} \propto \frac{\eta}{1-\eta}$, [25]). On the other hand, the packing density (porosity) also influences the sensitivity pattern of ΔT_0. For Sph1-HS at a low displacement velocity in Fig. 9 (b), the ΔT_0 is significantly smaller due to the larger relative dead volume that is defined in Refs. [61,62]. To summarize, the non-bonded La(Fe,Mn,Si)$_{13}$H$_y$ regenerators can potentially operate in a wider range than the epoxy-bonded regenerators.

The cooling curves [63], which describe the relations of specific cooling capacity versus temperature span, are shown in Fig. 10 for Epo-HS, Sph1-HS, Sph3-HS, and Irr3-H by varying the fluid displacement stroke. All the curves exhibit a near-linear trend with a lower slope at a lower temperature span, which is similar to previously reported results [64]. The reason is probably attributed to the temperature-dependent
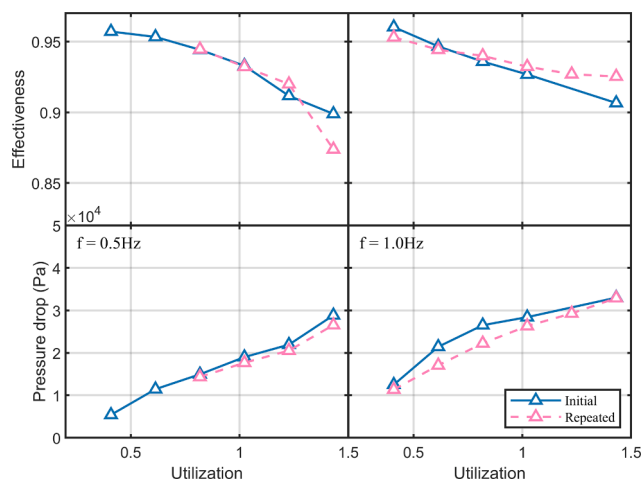

Fig. 11. Comparison of heat transfer effectiveness and pressure drop with respect to the utilization before and after the passive and active tests for Sph1-HS.

MCE of the MCM [65]. The hot reservoir temperature is set constant to ~ 20 °C for all test cases. As shown in Fig. 4, the transition temperatures of the materials used in these tests is within 1 K, and the hot reservoir temperature represents a good operating range for both that CALORIVAC -HS and -H materials. Consequently, the no-load temperature span in Fig. 10 is not necessarily the optimal one in Fig. 8. For each cooling power in Fig. 10, the corresponding temperature span has a single maximum as a function of utilization. At a low temperature span, the Epo-HS and Irr3-H obtained relatively high cooling capacity. The reasons are: (i) less internal dead volume losses for Epo-HS; and (ii) more intense MCE for Irr3-H over a narrow temperature span. Comparing the cooling curves for different AMRs with optimized utilization, the Sph3-HS regenerator outperformed the other AMRs as a whole, especially for temperature spans greater than 4 K. The specific cooling capacities for Epo-HS, Sph1-HS, Irr3-H, and Sph3-HS at a span of 4 K are 37, 38, 42 and 47 W/kg, respectively.

4.4. Stability evaluation

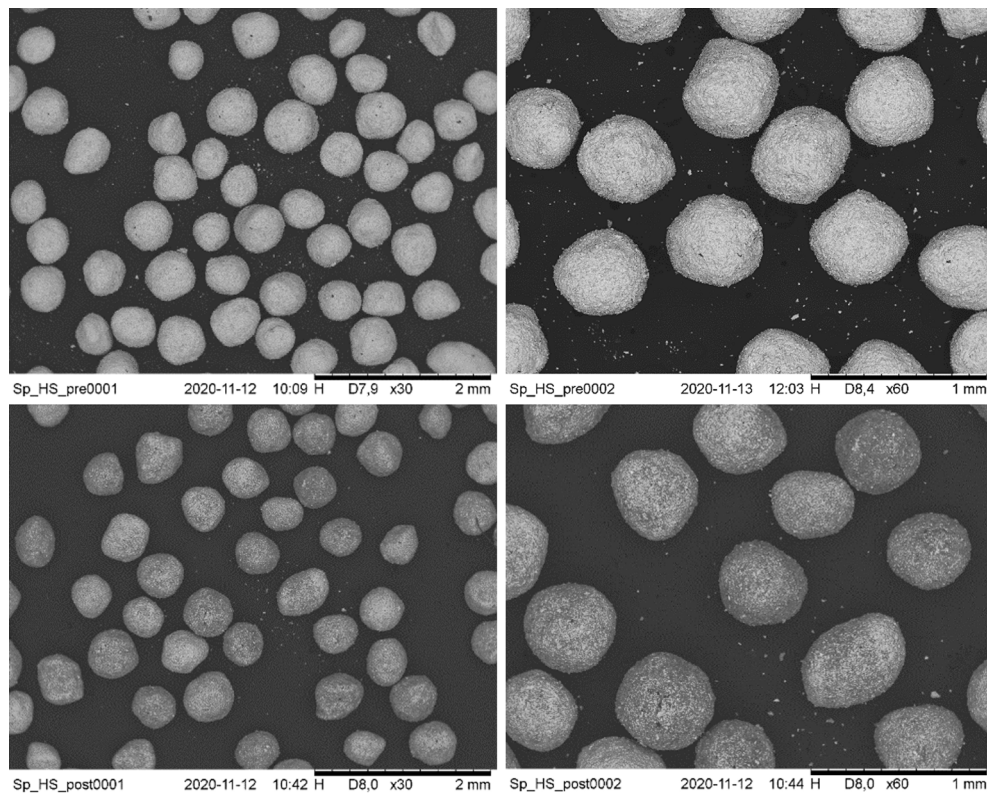For CALORIVAC-H previous studies have shown that irregular

Fig. 12. SEM images of the Sph1-HS material before and after the passive and active tests.

particle regenerators disintegrated after tests of a few weeks, both for the non-bonded case[36] and for a 1% wt. epoxy-bonded regenerator [37]. In this study, a similar phenomenon was observed for Irr3-H. Very fine powders were continuously generated and could be noticed during each replacement of heat transfer fluid, which indicates that some possible friction or collision between particles exists due to the magnetovolume effect.

In the cases of regenerators with CALORIVAC-HS, no fine powders could be observed by eye. The mechanical stability of CALORIVAC-HS particles was evaluated by re-measurement of heat transfer effectiveness and pressure drop for Sph1-HS for two frequencies (see Fig. 11). The timeline for the repeated passive experiments is shown in Fig. 5. Overall, the repeated curves of effectiveness and pressure drop (dashed lines) appear similar to the original curves (solid lines). This implies that the packing quality and channel profile of Sph1-HS can withstand the periodic magnetic forces and fluid flow, as well as prolonged dwell-time. Furthermore, the sufficiently good performance of reproduced Sph2-HS and Sph3-HS in Figs. 8-10 also indicates the stability of performance for CALORIVAC-HS materials. Additionally, SEM images from the CALORIVAC-HS material before and after the passive and active tests confirm its good mechanical integrity, as particles did not break apart during testing and retained their shape (see Fig. 12). The darker appearance of the Sph1-HS particles after testing is probably residue from the ENTEK corrosion inhibitor used during testing.

5. Conclusion and outlook

Non-epoxy-bonded regenerators with a stabilized first-order magnetocaloric material have been successfully tested for more than one year without observable performance reduction. The mechanical and chemical stabilities are validated via the comparison of specific heat, effectiveness and pressure drop before and after the passive and active characterizations. The regenerators are made from La(Fe,Mn,Si)$_{13}$H$_y$ stabilized through increasing the $\alpha - Fe$ content, which reduces the

adiabatic temperature change by around 10% under the magnetic field change from 0 to ~ 1 Tesla. Based on the component-level characterization, the performance of non-bonded regenerators can be summarized as follows.

(1) A non-bonded regenerator with high packing density shows a promising temperature span of 10.2 K for a single-layer of active magnetic regenerator with a first-order material.
(2) The non-bonded regenerator exhibits a significantly lower friction factor than the epoxy-bonded regenerator with the same particles due to the increased availability of fluid channels.
(3) The non-bonded regenerator, with high packing quality, showed a 27% higher cooling capacity than the epoxy-bonded one with the same materials and 12% higher than the packed irregular particle one, both at a temperature span of 4 K.

The paper described the potential of high stability and considerable performance for the non-bonded regenerators with first-order materials. The next step that can be reasonably expected is a flexible packing design of multi-layer magnetocaloric materials, which would result in higher efficiency.

Declaration of Competing Interest

The authors declare that they have no known competing financial interests or personal relationships that could have appeared to influence the work reported in this paper.

Acknowledgments

References

[1] J. Kalizan, J. Tušek, Caloric Micro-Cooling: Numerical modelling and parametric investigation, Energy Convers. Manag. 225 (2020) 113421, https://doi.org/10.1016/j.enconman.2020.113421.

[2] C. Aprea, A. Greco, A. Maiorino, C. Masselli, The employment of caloric-effect materials for solid-state heat pumping, Int. J. Refrig. 109 (2020) 1–11, https://doi.org/10.1016/j.ijrefrig.2019.09.011.

[3] A. Greco, C. Aprea, A. Maiorino, C. Masselli, Int. J. Refrig. 106 (2019) 66–88, https://doi.org/10.1016/j.ijrefrig.2019.06.034.

[4] A. Czernuszewicz, J. Kaleta, D. Lewandowski, Multicaloric effect: Toward a breakthrough in cooling technology, Energy Convers. Manag. 178 (2018) 335–342, https://doi.org/10.1016/j.enconman.2018.10.025.

[5] C. Aprea, A. Greco, A. Maiorino, C. Masselli, Solid-state refrigeration: A comparison of the energy performances of caloric materials operating in an active caloric regenerator, Energy. 165 (2018) 439–455, https://doi.org/10.1016/j.energy.2018.09.114.

[6] A. Kitanovski, Energy Applications of Magnetocaloric Materials, Adv. Energy Mater. 10 (10) (2020) 1903741, https://doi.org/10.1002/aenm.v10.1010.1002/aenm.201903741.

[7] T. Gottschall, K.P. Skokov, M. Fries, A. Taubel, I. Radulov, F. Scheibel, D. Benke, S. Riegg, O. Gutfleisch, Making a Cool Choice: The Materials Library of Magnetic Refrigeration, Adv. Energy Mater. 9 (34) (2019) 1901322, https://doi.org/10.1002/aenm.v9.3410.1002/aenm.201901322.

[8] V. Chaudhary, X. Chen, R.V. Ramanujan, Iron and manganese based magnetocaloric materials for near room temperature thermal management, Prog. Mater. Sci. 100 (2019) 64–98, https://doi.org/10.1016/j.pmatsci.2018.09.005.

[9] V. Franco, J.S. Blázquez, J.J. Ipus, J.Y. Law, L.M. Moreno-Ramírez, A. Conde, Magnetocaloric effect: From materials research to refrigeration devices, Prog. Mater. Sci. 93 (2018) 112–232, https://doi.org/10.1016/j.pmatsci.2017.10.005.

[10] K. Klinar, U. Tomc, B. Jelenc, S. Nosan, A. Kitanovski, New frontiers in magnetic refrigeration with high oscillation energy-efficient electromagnets, Appl. Energy. 236 (2019) 1062–1077, https://doi.org/10.1016/j.apenergy.2018.12.055.

[11] F.P. Fortkamp, J.A. Lozano, J.R. Barbosa, Analytical solution of concentric two-pole Halbach cylinders as a preliminary design tool for magnetic refrigeration systems, J. Magn. Magn. Mater. 444 (2017) 87–97, https://doi.org/10.1016/j.jmmm.2017.07.072.

[12] J. Lee, J. Lee, Magnetic force enhancement using air-gap magnetic field manipulation by optimized coil currents, Appl. Sci. 10 (1) (2020) 104, https://doi.org/10.3390/app10010104.

[13] A. Kitanovski, J. Tušek, U. Tomc, U. Plaznik, M. Ožbolt, A. Poredoš, Magnetocaloric Energy Conversion: From Theory to Applications (2015), https://doi.org/10.1007/978-3-319-08741-2.

[14] J. Romero Gómez, R. Ferreiro Garcia, A. De Miguel Catoira, M. Romero Gómez, Magnetocaloric effect: A review of the thermodynamic cycles in magnetic refrigeration, Renew. Sustain. Energy Rev. 17 (2013) 74–82, https://doi.org/10.1016/j.rser.2012.09.027.

[15] J. He, J. Wu, B. Lu, C. Liu, Comparative study on the series, parallel and cascade cycles of a multi-mode room temperature magnetic refrigeration system, Int. J. Refrig. 117 (2020) 94–103, https://doi.org/10.1016/j.ijrefrig.2020.04.011.

[16] M.S. Kamran, H.O. Ahmad, H.S. Wang, Review on the developments of active magnetic regenerator refrigerators – Evaluated by performance, Renew. Sustain. Energy Rev. 133 (2020) 110247, https://doi.org/10.1016/j.rser.2020.110247.

[17] S. Lionte, M. Risser, C. Muller, A 15kW magnetocaloric proof-of-concept unit: Initial development and first experimental results, Int. J. Refrig. 122 (2021) 256–265, https://doi.org/10.1016/j.ijrefrig.2020.09.019.

[18] C.R.H. Bahl, K. Engelbrecht, D. Eriksen, J.A. Lozano, R. Bjørk, J. Geyti, K. K. Nielsen, A. Smith, N. Pryds, Development and experimental results from a 1 kW prototype AMR, Int. J. Refrig. 37 (2014) 78–83, https://doi.org/10.1016/j.ijrefrig.2013.09.001.

[19] S. Jacobs, J. Auringer, A. Boeder, J. Chell, L. Komorowski, J. Leonard, S. Russek, C. Zimm, The performance of a large-scale rotary magnetic refrigerator, Int. J. Refrig. 37 (2014) 84–91, https://doi.org/10.1016/j.ijrefrig.2013.09.025.

[20] A.T.D. Nakashima, F.P. Fortkamp, N.M. de Sá, V.M.A. dos Santos, G. Hoffmann, G. F. Peixer, S.L. Dutra, M.C. Ribeiro, J.A. Lozano, J.R. Barbosa, A Magnetic Wine Cooler Prototype, Int. J. Refrig. 122 (2021) 110–121, https://doi.org/10.1016/j.ijrefrig.2020.11.015.

[21] J.A. Barclay, W.A. Steyert, Active magnetic regenerator, US-Patent 4332135A, 1982.

[22] S. Qian, J. Yu, G. Yan, A review of regenerative heat exchange methods for various cooling technologies, Renew. Sustain. Energy Rev. 69 (2017) 535–550, https://doi.org/10.1016/j.rser.2016.11.180.

[23] P.V. Trevizoli, R. Teyber, P.S. da Silveira, F. Scharf, S.M. Schillo, I. Niknia, P. Govindappa, T.V. Christiaanse, A. Rowe, Thermal-hydraulic evaluation of 3D printed microstructures, Appl. Therm. Eng. 160 (2019) 113990, https://doi.org/10.1016/j.applthermaleng.2019.113990.

[24] P.V. Trevizoli, G.F. Peixer, J.R. Barbosa, Thermal-hydraulic evaluation of oscillating-flow regenerators using water: Experimental analysis of packed beds of spheres, Int. J. Heat Mass Transf. 99 (2016) 918–930, https://doi.org/10.1016/j.ijheatmasstransfer.2016.03.014.

[25] J. Liang, K.K. Nielsen, K. Engelbrecht, C.R.H. Bahl, Heat transfer figures of merit for mapping passive regenerator performance to active regenerator cooling power, Appl. Therm. Eng. 181 (2020) 115993, https://doi.org/10.1016/j.applthermaleng.2020.115993.

[26] T. Lei, K. Navickaitė, K. Engelbrecht, A. Barcza, H. Vieyra, K.K. Nielsen, C.R. H. Bahl, Passive characterization and active testing of epoxy bonded regenerators for room temperature magnetic refrigeration, Appl. Therm. Eng. 128 (2018) 10–19, https://doi.org/10.1016/j.applthermaleng.2017.08.152.

[27] J. Tušek, A. Kitanovski, U. Tomc, C. Favero, A. Poredoš, Experimental comparison of multi-layered La-Fe-Co-Si and single-layered Gd active magnetic regenerators for use in a room-temperature magnetic refrigerator, Int. J. Refrig. 37 (2014) 117–126, https://doi.org/10.1016/j.ijrefrig.2013.09.003.

[28] K. Navickaitė, J. Liang, C. Bahl, S. Wieland, T. Buchenau, K. Engelbrecht, Experimental characterization of active magnetic regenerators constructed using laser beam melting technique, Appl. Therm. Eng. 174 (2020) 115297, https://doi.org/10.1016/j.applthermaleng.2020.115297.

[29] Z. Li, J. Shen, K. Li, X. Gao, X. Guo, W. Dai, Assessment of three different gadolinium-based regenerators in a rotary-type magnetic refrigerator, Appl. Therm. Eng. 153 (2019) 159–167, https://doi.org/10.1016/j.applthermaleng.2019.02.100.

[30] J. Lyubina, Magnetocaloric materials for energy efficient cooling, J. Phys. D. Appl. Phys. 50 (5) (2017) 053002, https://doi.org/10.1088/1361-6463/50/5/053002.

[31] T.V. Christiaanse, P.V. Trevizoli, S. Misra, C. Carroll, D. van Asten, L. Zhang, R. Teyber, P. Govindappa, I. Niknia, A. Rowe, Experimental study of 2-layer regenerators using Mn-Fe-Si-P materials, J. Phys. D. Appl. Phys. 51 (10) (2018) 105002, https://doi.org/10.1088/1361-6463/aaaba7.

[32] M. Zhang, O. Abdelaziz, A.M. Momen, A. Abu-Heiba, A numerical analysis of a magnetocaloric refrigerator with a 16-layer regenerator, Sci. Rep. 7 (2017) 1–12, https://doi.org/10.1038/s41598-017-14406-9.

[33] P. Govindappa, P.V. Trevizoli, O. Campbell, I. Niknia, T.V. Christiaanse, R. Teyber, S. Misra, M.A. Schwind, D. van Asten, L. Zhang, A. Rowe, Experimental investigation of MnFeP 1–x As x multilayer active magnetic regenerators, J. Phys. D. Appl. Phys. 50 (31) (2017) 315001, https://doi.org/10.1088/1361-6463/aa7a33.

[34] A. Barcza, M. Katter, V. Zellmann, S. Russek, S. Jacobs, C. Zimm, Stability and magnetocaloric properties of sintered La(Fe, Mn, Si) 13Hz alloys, IEEE Trans. Magn. (2011), https://doi.org/10.1109/TMAG.2011.2147774.

[35] C. Aprea, A. Greco, A. Maiorino, C. Masselli, Magnetic refrigeration: An eco-friendly technology for the refrigeration at room temperature, J. Phys. Conf. Ser. 655 (2015) 012026, https://doi.org/10.1088/1742-6596/655/1/012026.

[36] H.N. Bez, K. Navickaite, T. Lei, K. Engelbrecht, A. Barcza, C.R.H. Bahl, Epoxy-bonded La(Fe, Mn, Si)13Hzas a multi layered active magnetic regenerator, Refrig. Sci. Technol. (2016), https://doi.org/10.18462/iir.thermag.2016.0147.

[37] K. Navickaitė, H.N. Bez, T. Lei, A. Barcza, H. Vieyra, C.R.H. Bahl, K. Engelbrecht, Experimental and numerical comparison of multi-layered La(Fe, Si, Mn)13Hy active magnetic regenerators, Int. J. Refrig. 86 (2018) 322–330, https://doi.org/10.1016/j.ijrefrig.2017.10.032.

[38] B.P. Vieira, H.N. Bez, M. Kuepferling, M.A. Rosa, D. Schafer, C.C. Plá Cid, H. A. Vieyra, V. Basso, J.A. Lozano, J.R. Barbosa Jr., Magnetocaloric properties of spheroidal La(Fe, Mn, Si)13Hy granules and their performance in epoxy-bonded active magnetic regenerators, Appl. Therm. Eng. 183 (2021) 116185, https://doi.org/10.1016/j.applthermaleng.2020.116185.

[39] S. Wieland, F. Petzoldt, Powder-extrusion and sintering of magnetocaloric LaCe (FeMnSi)13 alloy, J. Alloys Compd. 719 (2017) 182–188, https://doi.org/10.1016/j.jallcom.2017.05.168.

[40] I.A. Radulov, K.P. Skokov, D.Y. Karpenkov, T. Braun, O. Gutfleisch, T.U. Darmstadt, Polymer-Bonded La (Fe , Mn , Si) 13 H x Plates for Heat Exchangers 51 (2015) 11–14.

[41] H. Neves Bez, K.K. Nielsen, A. Smith, P. Norby, K. Ståhl, C.R.H. Bahl, Strain development during the phase transition of La(Fe,Mn,Si)13Hz, Appl. Phys. Lett. 109 (2016). doi:10.1063/1.4960358.

[42] I.A. Radulov, D.Y. Karpenkov, K.P. Skokov, A.Y. Karpenkov, T. Braun, V. Brabänder, T. Gottschall, M. Pabst, B. Stoll, O. Gutfleisch, Production and properties of metal-bonded La(Fe, Mn, Si)13Hx composite material, Acta Mater. 127 (2017) 389–399, https://doi.org/10.1016/j.actamat.2017.01.054.

[43] I.A. Radulov, D.Y. Karpenkov, M. Specht, T. Braun, A.Y. Karpenkov, K.P. Skokov, O. Gutfleisch, T.U. Darmstadt, A. Characterization, Heat Exchangers From Metal-Bonded La (Fe , Mn , Si) 13 H x Powder 53 (2017) 1–7.

[44] I. Titov, M. Acet, M. Farle, D. González-Alonso, L. Mañosa, A. Planes, T. Krenke, Hysteresis effects in the inverse magnetocaloric effect in martensitic Ni-Mn-In and Ni-Mn-Sn, J. Appl. Phys. 112 (7) (2012) 073914, https://doi.org/10.1063/1.4757425.

[45] A.G. Gamzatov, A.M. Aliev, A. Ghotbi Varzaneh, P. Kameli, I. Abdolhosseini Sarsari, S.C. Yu, Inverse-direct magnetocaloric effect crossover in Ni 47 Mn 40 Sn 12.5 Cu 0.5 Heusler alloy in cyclic magnetic fields, Appl. Phys. Lett. 113 (17) (2018) 172406, https://doi.org/10.1063/1.5049398.

[46] M. Bratko, E. Lovell, A.D. Caplin, V. Basso, A. Barcza, M. Katter, L.F. Cohen, Determining the first-order character of La(Fe, Mn, Si)13, Phys. Rev. B. 95 (2017) 1–8, https://doi.org/10.1103/PhysRevB.95.064411.

[47] V. Basso, M. Küpferling, C. Curcio, C. Bennati, A. Barzca, M. Katter, M. Bratko, E. Lovell, J. Turcaud, L.F. Cohen, Specific heat and entropy change at the first order phase transition of La(Fe-Mn-Si)13H compounds, J. Appl. Phys. 118 (5) (2015) 053907, https://doi.org/10.1063/1.4928086.

[48] T. Lei, Modeling of active magnetic regenerators and experimental investigation of passive regenerators with oscillating flow, Technical University of Denmark, 2016.

[49] J. Liang, C. Christiansen, K. Engelbrecht, K.K. Nielsen, R. Bjørk, C.R.H. Bahl, Heat transfer and flow resistance analysis of a novel freeze-cast regenerator, Int. J. Heat Mass Transf. 155 (2020) 119772, https://doi.org/10.1016/j.ijheatmasstransfer.2020.119772.

[50] C.R.H. Bahl, T.F. Petersen, N. Pryds, A. Smith, A versatile magnetic refrigeration test device, Rev. Sci. Instrum. 79 (9) (2008) 093906, https://doi.org/10.1063/1.2981692.

[51] P.V. Trevizoli, J.R. Barbosa, R.T.S. Ferreira, Experimental evaluation of a Gd-based linear reciprocating active magnetic regenerator test apparatus, Int. J. Refrig. 34 (6) (2011) 1518–1526, https://doi.org/10.1016/j.ijrefrig.2011.05.005.

[52] Y. Shao, J. Liu, M. Zhang, A. Yan, K.P. Skokov, D.Y. Karpenkov, O. Gutfleisch, High-performance solid-state cooling materials: Balancing magnetocaloric and non-magnetic properties in dual phase La-Fe-Si, Acta Mater. 125 (2017) 506–512, https://doi.org/10.1016/j.actamat.2016.12.014.

[53] F. Erbesdobler, C.R.H. Bahl, R. Bjørk, K.K. Nielsen, Detailed isofield calorimetry of La(Fe, Si, Mn)H reveals distributed magnetocaloric phase transitions, J. Appl. Phys. 127 (9) (2020) 095102, https://doi.org/10.1063/1.5137790.

[54] S. Jeppesen, Magnetocaloric materials, University of Copenhagen (2008), https://doi.org/10.1007/978-3-319-26106-5_4.

[55] K.K. Nielsen, H.N. Bez, L. von Moos, R. Bjørk, D. Eriksen, C.R.H. Bahl, Direct measurements of the magnetic entropy change, Rev. Sci. Instrum. 86 (10) (2015) 103903, https://doi.org/10.1063/1.4932308.

[56] B. Monfared, Design and optimization of regenerators of a rotary magnetic refrigeration device using a detailed simulation model, Int. J. Refrig. 88 (2018) 260–274, https://doi.org/10.1016/j.ijrefrig.2018.01.011.

[57] P.V. Trevizoli, A.T. Nakashima, G.F. Peixer, J.R. Barbosa, Performance assessment of different porous matrix geometries for active magnetic regenerators, Appl. Energy. 187 (2017) 847–861, https://doi.org/10.1016/j.apenergy.2016.11.031.

[58] J. Liang, C.D. Christiansen, K. Engelbrecht, K.K. Nielsen, R. Bjørk, C.R.H. Bahl, Heat transfer and flow resistance analysis of a novel freeze-cast regenerator, Int. J. Heat Mass Transf. 155 (2020) 119772, https://doi.org/10.1016/j.ijheatmasstransfer.2020.119772.

[59] K. Engelbrecht, C.R.H. Bahl, K.K. Nielsen, Experimental results for a magnetic refrigerator using three different types of magnetocaloric material regenerators, Int. J. Refrig. 34 (4) (2011) 1132–1140, https://doi.org/10.1016/j.ijrefrig.2010.11.014.

[60] U. Legait, F. Guillou, A. Kedous-Lebouc, V. Hardy, M. Almanza, An experimental comparison of four magnetocaloric regenerators using three different materials, Int. J. Refrig. 37 (2013) 147–155, https://doi.org/10.1016/j.ijrefrig.2013.07.006.

[61] Y. Liu, Dead Volume Effects in Passive Regeneration : Experimental and Numerical Characterization, University of Victoria (2015).

[62] P.V. Trevizoli, A.T. Nakashima, J.R. Barbosa, Performance evaluation of an active magnetic regenerator for cooling applications – part II: Mathematical modeling and thermal losses, Int. J. Refrig. 72 (2016) 206–217, https://doi.org/10.1016/j.ijrefrig.2016.07.010.

[63] A. Rowe, Configuration and performance analysis of magnetic refrigerators, Int. J. Refrig. 34 (1) (2011) 168–177, https://doi.org/10.1016/j.ijrefrig.2010.08.014.

[64] P.V. Trevizoli, A.T. Nakashima, G.F. Peixer, J.R. Barbosa, Performance evaluation of an active magnetic regenerator for cooling applications – part I: Experimental analysis and thermodynamic performance, Int. J. Refrig. 72 (2016) 192–205, https://doi.org/10.1016/j.ijrefrig.2016.07.009.

[65] M.A. Benedict, S.A. Sherif, M. Schroeder, D.G. Beers, Experimental impact of magnet and regenerator design on the refrigeration performance of first- order magnetocaloric materials, Int. J. Refrig. 74 (2017) 188–197, https://doi.org/10.1016/j.ijrefrig.2016.09.023.